Catalysis and chemical mechanisms of calcite dissolution in seawater

Adam V. Subhas[a,1], Jess F. Adkins[a], Nick E. Rollins[b], John Naviaux[a], Jonathan Erez[c], and William M. Berelson[b]

[a]Division of Geological and Planetary Sciences, California Institute of Technology, Pasadena, CA 91125; [b]Department of Earth Sciences, University of Southern California, Los Angeles, CA 90089; and [c]Institute of Earth Sciences, Hebrew University of Jerusalem, Jerusalem 9190401, Israel

Edited by Mark H. Thiemens, University of California, San Diego, La Jolla, CA, and approved June 26, 2017 (received for review March 6, 2017)

Near-equilibrium calcite dissolution in seawater contributes significantly to the regulation of atmospheric CO_2 on 1,000-y timescales. Despite many studies on far-from-equilibrium dissolution, little is known about the detailed mechanisms responsible for calcite dissolution in seawater. In this paper, we dissolve ^{13}C-labeled calcites in natural seawater. We show that the time-evolving enrichment of $\delta^{13}C$ in solution is a direct measure of both dissolution and precipitation reactions across a large range of saturation states. Secondary Ion Mass Spectrometer profiles into the ^{13}C-labeled solids confirm the presence of precipitated material even in undersaturated conditions. The close balance of precipitation and dissolution near equilibrium can alter the chemical composition of calcite deeper than one monolayer into the crystal. This balance of dissolution–precipitation shifts significantly toward a dissolution-dominated mechanism below about $\Omega = 0.7$. Finally, we show that the enzyme carbonic anhydrase (CA) increases the dissolution rate across all saturation states, and the effect is most pronounced close to equilibrium. This finding suggests that the rate of hydration of CO_2 is a rate-limiting step for calcite dissolution in seawater. We then interpret our dissolution data in a framework that incorporates both solution chemistry and geometric constraints on the calcite solid. Near equilibrium, this framework demonstrates a lowered free energy barrier at the solid–solution interface in the presence of CA. This framework also indicates a significant change in dissolution mechanism at $\Omega = 0.7$, which we interpret as the onset of homogeneous etch pit nucleation.

mineral dissolution | isotope geochemistry | oceanography | catalysis

The production and dissolution of calcium carbonate minerals provide a crucial link between the marine carbon and alkalinity cycles. The ocean has absorbed about 25 to 30% of anthropogenic CO_2 emissions, dropping mean surface ocean pH since the industrial era (1). As ocean pH decreases, sedimentary carbonate minerals will dissolve to compensate for the loss of buffering capacity, eventually restoring atmospheric pCO_2 to about its preindustrial level (2, 3). This reaction will mostly take place in the deep ocean, where the calcite saturation state $\Omega = [Ca^{2+}][CO_3^{2-}]/K'_{sp} < 1$. Most of the deep ocean is only mildly undersaturated such that pelagic dissolution is primarily a near-equilibrium phenomenon. However, attempts to quantify the relationship between calcite dissolution rate and Ω are highly variable between different studies, both in functional form and absolute value (4–9).

With the exception of very early work by Berner and Morse (7), few studies have attempted to unpack the chemical species responsible for calcite dissolution in seawater. Many studies choose instead to derive empirical relationships between saturation state and dissolution rate (5, 6, 10, 11). In contrast, freshwater and dilute solution dissolution studies have made large advances in identifying key chemical species responsible for observed dissolution rates, starting from early work (12–14) and culminating in a dissolution model that incorporates both aqueous species and the distribution of ion complexes on the calcite surface (15, 16). These groups recover an essentially linear relationship between dissolution rate and saturation state.

Calcite dissolution rates in freshwater under circumneutral pH conditions appear largely independent of solution pH (10), but instead respond nonlinearly to mineral surface processes (17–20). For example, faster dissolution rates are typically associated with a large increase in etch pit nucleation below some critical saturation state, $\Omega_{critical}$ (21, 22). Even in freshwater, however, a link between the generation of etch pits and other surface features, and the overlying solution chemistry, is poorly understood (20).

In this paper, we use a method that unpacks the relationship between calcite dissolution kinetics and seawater chemistry (*Methods* and ref. 9). In short, ^{13}C-labeled calcites are placed in undersaturated seawater in a closed system with no headspace. The evolving seawater $\delta^{13}C$ traces mass transfer from solid to solution. Dissolution will add ^{13}C to solution; precipitation will add seawater carbon ($\sim$99% ^{12}C) to the solid surface. We first demonstrate precipitation in undersaturated solutions using Secondary Ion Mass Spectrometry (SIMS) analysis of the calcite solid. Next, we show that a box model of calcite dissolution and precipitation provides information about gross precipitation and dissolution fluxes at the calcite surface near equilibrium. The model predicts a decrease in relative importance of precipitation below $\Omega = 0.7$. Finally, we show that the enzyme carbonic anhydrase (CA) catalyzes the dissolution of calcite in seawater. CA is a cosmopolitan enzyme known for its rapid equilibration of carbonic acid and aqueous CO_2. A mechanism of dissolution through defect-assisted etch pit nucleation (21) is proposed, which also demonstrates a distinct change in reaction energetics at $\Omega = 0.7$. Near equilibrium, CA reduces the free energy barrier to dissolution. At high [CA], this energy barrier is similar to that recovered from freshwater dissolution experiments.

Significance

The experimental system described here provides constraints on the relative balance of gross dissolution and precipitation fluxes contributing to the observed net dissolution rate of calcite in seawater. We show that our dissolution rates fit well within a framework that accounts for the geometry of the dissolving mineral surface. We further show that carbonic anhydrase (CA) catalyzes calcite dissolution, which implicates the hydration of aqueous CO_2 as a rate-limiting step for calcite dissolution in seawater. The presence of carbonic anhydrase in carbonate-rich environments such as coral reefs or sinking marine particles is poorly understood. However, our findings suggest that CA activity would significantly enhance the rate at which alkalinity is cycled between solids and seawater in these environments.

Author contributions: A.V.S., J.F.A., N.E.R., J.E., and W.M.B. designed research; A.V.S., N.E.R., and J.N. performed research; A.V.S., J.F.A., N.E.R., J.N., and W.M.B. analyzed data; and A.V.S., J.F.A., J.N., and W.M.B. wrote the paper.

The authors declare no conflict of interest.

This article is a PNAS Direct Submission.

[1]To whom correspondence should be addressed. Email: asubhas@gps.caltech.edu.

This article contains supporting information online at www.pnas.org/lookup/suppl/doi:10.1073/pnas.1703604114/-/DCSupplemental.

Measuring Dissolution–Precipitation in the Calcite Solid

The net rate of $CaCO_3$ dissolution is the result of a balance between dissolution and precipitation reactions near equilibrium. Our experimental system has a strong isotopic gradient between seawater and the ^{13}C-labeled mineral, such that the processes of precipitation and dissolution will each leave distinct isotopic signatures on the solid. Seawater ^{12}C will precipitate and increase the $^{12}C/^{13}C$ ratio of the reactive calcite surface. Dissolution will expose pure ^{13}C carbonate such that the surface composition approaches 100% ^{13}C as dissolution outpaces precipitation at lower saturation state. A change in Mg/Ca should also be measurable because the initial calcite mineral contains only trace Mg^{2+}.

We measured the near-equilibrium balance of dissolution and precipitation by reacting several ^{13}C-labeled, Mg-free calcites for 48 h in saturated and slightly undersaturated seawater. Using SIMS, we then measured carbon isotope and Mg/Ca profiles through this reacted surface and compared them to an unreacted control (Fig. 1 and *SI Appendix*, Fig. S1). The unreacted control experiments (dashed yellow) show some enrichment of ^{12}C due to surface contamination. The supersaturated experiments (dotted blue), which will have precipitated calcite, show persistent ^{12}C and Mg/Ca enrichment above the unreacted control. The undersaturated experiments (solid red) start at a surface composition similar to precipitated calcite, indicating that ^{12}C has been incorporated even in undersaturated conditions. Undersaturated profiles then transition down to the composition of the unreacted control, matching the unreacted pure ^{13}C calcite composition at a depth of about 4 nm. Fig. 1, *Inset* shows that all $^{12}C/^{13}C$ compositions converge within error at about 130 nm deep, indicating that underlying ^{13}C calcium carbonate has been reached.

The shape of these SIMS profiles is influenced by the incorporation of ^{12}C from precipitation, and also by the mixing of surface signals down into the calcite interior during secondary ion sputtering and excavation. To more quantitatively measure the total number of moles of seawater C and Mg^{2+} incorporated into our calcites, we integrated each of the curves in Fig. 1 and *SI Appendix*, Fig. S1 over the 140-nm SIMS profile (*SI Appendix*, Eqs. **S1** and **S2** and Table S2). This integral can be converted to a "reactive thickness" and compared with previous estimates. Briefly, the measured $^{12}C/^{13}C$ mole fraction measured at each SIMS analysis cycle was converted to a number of moles of ^{12}C. All cycles were then summed over the entire profile to estimate the total number of moles of ^{12}C incorporated into our calcites over the 48-h experimental period. To remove the influence of surface contamination, the control was subtracted from both the supersaturated and undersaturated experiments. The total number of moles was then converted into an effective thickness of ^{12}C present in the supersaturated and undersaturated experiments (*SI Appendix*, Table S2). This calculation estimates that 1.0 nm to 3.3 nm of ^{12}C calcite was incorporated in undersaturated conditions. Mg/Ca measurements also confirm the presence of new Mg^{2+} in the solid (*SI Appendix*, Table S2). We also found that 3.1 nm to 9.3 nm of ^{12}C calcite was added in supersaturated experiments, in agreement with previous precipitation experiments (ref. 23 and *SI Appendix*, Fig. S3). One calcite monolayer is about 0.5 nm, suggesting that, even under conditions of net dissolution, seawater can react with two to six monolayers of calcite via gross dissolution and precipitation reactions.

Most calcite dissolution in the deep sea happens near equilibrium, where we have documented a large influence of dissolution and precipitation reactions on the composition of the calcite surface. Calcites in sediments, which contain primary environmental information in their oxygen isotope and/or Mg/Ca ratios, will experience similar dissolution–precipitation reactions in the deep ocean (24–26). These reactions will impart secondary porewater isotopic and chemical information, and our experiments suggest they can potentially do so deeply into the calcite surface.

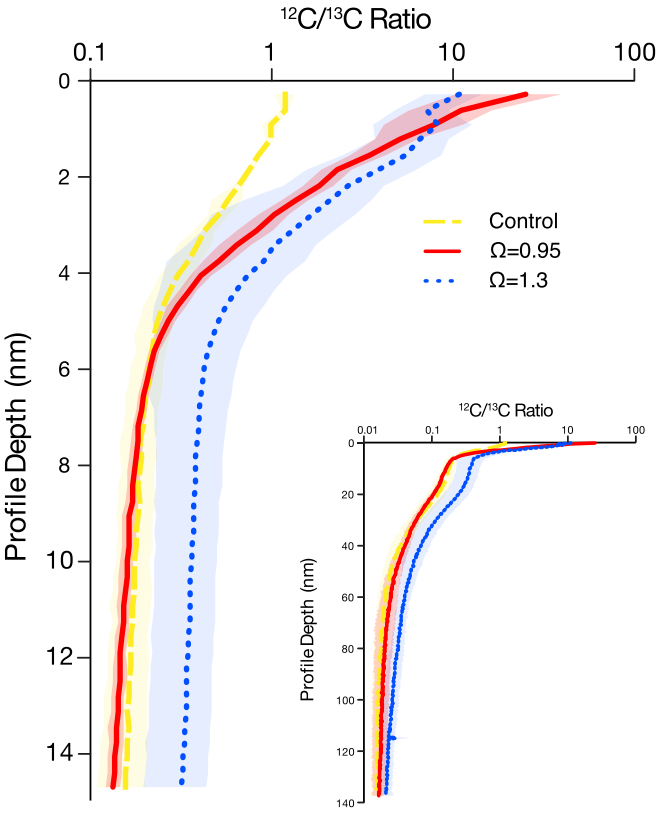

Fig. 1. Vertical logarithmic $^{12}C/^{13}C$ SIMS profiles of reacted calcite grains under three different experimental conditions. Solid lines are the mean isotope ratio of all profiles collected under each experimental condition. Shaded areas are the SD of all profiles collected under each experimental condition. In the first 15 nm of these profiles, Ω =0.95 profiles (solid red) transition from a supersaturated (dotted blue) composition to an unreacted (dashed yellow) composition. This ^{12}C enrichment demonstrates that seawater carbon has incorporated into the calcite solid in undersaturated conditions. (*Inset*) SIMS entire profile, with experiment ratios converging with the unreacted control run at depth. All curves are depth-corrected for the thickness of gold coating. Note that the *x* axis is flipped relative to the convention of plotting a $^{13}C/^{12}C$ ratio.

Future work will target understanding the extent to which these processes modify deep-sea sedimentary calcites, and should prove useful in unmixing the secondary and primary environmental signals that these calcites record.

Measuring and Modeling Dissolution–Precipitation in the Solution

In addition to measuring dissolution–precipitation reactions in the solid, we measured the appearance of ^{13}C in seawater dissolved inorganic carbon (DIC) using a Picarro cavity ring-down spectrometer (9). The dissolution of ^{13}C calcite produces a linear increase of seawater $\delta^{13}C$ over time. The slope of this line is a direct measure of the net dissolution rate (e.g., rates in ref. 9). However, we also observe curvature in plots of $\delta^{13}C$ versus time (Fig. 2). Because an experiment is conducted at a fixed saturation state and mineral surface area, curvature in Fig. 2*B* cannot represent a change in bulk solution chemistry, but instead reflects the instantaneous balance of fixed dissolution and precipitation rates at the mineral surface. Precipitation adds ^{12}C to the solid surface, which changes the isotopic composition of the dissolving solid. The calcite surface will continue to change its $^{13}C/^{12}C$ ratio until it comes into steady state with respect to gross dissolution and precipitation reactions. Curves of $\delta^{13}C$ versus time thus straighten out when the calcite surface comes into steady

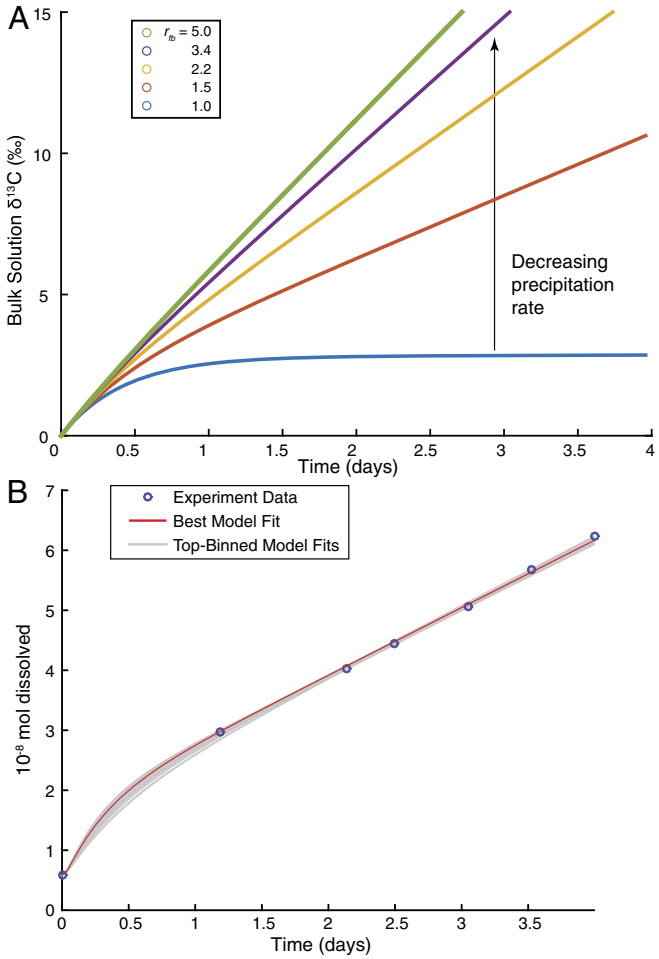

Fig. 2. Results of the dissolution–precipitation model (*SI Appendix*, Fig. S3 and Eqs. S2–S4). (*A*) Model output of bulk solution $\delta^{13}C$ under our experimental conditions, assuming a reactive calcite layer thickness of five monolayers. Decreasing the precipitation rate (increasing r_{bf}; see *Measuring and Modeling Dissolution–Precipitation in the Solution* for details) increases the net dissolution rate and decreases curvature. (*B*) Model–data comparison for a dissolution experiment conducted at $\Omega = 0.87$. The red curve is the absolute best-fit k_{diss} and r_{fb} over the entire parameter search space; the gray curves are the next 15 best fits.

state with respect to these dissolution and precipitation fluxes (Fig. 2*A*). Using the observation of precipitated calcite even in undersaturated conditions, we developed a box model to quantify the impact of dissolution and precipitation reactions on solution $\delta^{13}C$ versus time (see *SI Appendix*, Fig. S4 for model description).

All experimental data with sufficient data density from ref. 9 were fit with output from the box model. We modeled a suite of dissolution rate curves over a range of gross dissolution (R_f) and precipitation rates (R_b). The magnitude of these rates, and their ratio ($r_{fb} = R_f/R_b$), sets the amount of initial curvature. For example, when $r_{fb} = 1$, the precipitation rate is equal to the dissolution rate, and calcite is in equilibrium with solution (the blue line in Fig. 2*A*). When $r_{fb} = 5$, the dissolution rate is 5 times faster than the precipitation rate (the green line in Fig. 2*A*). The size and shape of curvature observed in Fig. 2 is also set by the volume of calcite that is allowed to react with seawater. Consistent with our SIMS results, the model gives a better fit to the data if multiple monolayers of calcite are reacting with seawater, and gives a best fit with five monolayers (*SI Appendix*, Fig. S7). An example data fit using model output is shown in Fig. 2*B* and *SI Appendix*, Fig. S6; details of the fitting routine are in *SI Appendix*. Ranges of acceptable dissolution and precipitation rates were calculated from the acceptable model-fit R_f and r_{fb} values, shown as the spread of gray curves that adequately fit the dataset in Fig. 2*B*.

Dissolution studies in seawater have typically related net dissolution rate with undersaturation [$1 - \Omega$ (4, 6–8, 27, 28)]. This framework is historically linked to a derivation of net dissolution rate,

$$R_{diss} = R_f - R_b = k_f\{CaCO_3\} - k_b[Ca^{2+}][CO_3^{2-}], \qquad [1]$$

where R is a rate and k_f and k_b are the specific dissolution and precipitation rate constants, respectively. This expression, along with the assumption that activity of the solid is 1, defines a linear relationship between net dissolution and $1 - \Omega$ (see *SI Appendix* for derivation). Furthermore, the precipitation term in Eq. **1** is the only term that explicitly includes information about the concentrations of calcium and carbonate ion in solution. In other words, gross dissolution is independent of solution composition, and saturation state only affects the rate of gross precipitation. Such dissolution behavior has been demonstrated in freshwater (e.g., ref. 16), but has never been investigated directly in seawater. Our modeling results here are the complement to this freshwater approach. Model-fit gross dissolution and precipitation rates, shown in Fig. 3, cannot be fit using a constant dissolution rate and a decreasing precipitation rate, as predicted by the linear model of Eq. **1**. Instead, gross dissolution rates show a strong, nonlinear dependence on saturation state, changing by almost four orders of magnitude over the entire range of saturation states measured here. This nonlinearity implies that either the dissolution rate constant or the activity of the solid in Eq. **1** changes as a function of saturation state.

As undersaturation increases, the range of acceptable precipitation rates grows much larger than the range of acceptable dissolution rates, as shown by the size of the boxes in Fig. 3*A*. The ratio of gross dissolution to precipitation ($r_{fb} = R_f/R_b$) also significantly increases below about $\Omega = 0.7$, suggesting a decreased contribution of precipitation to the net dissolution rate farther from equilibrium (Fig. 3*B*). The linear dissolution framework (Eq. **1**) predicts a continuous decline in precipitation as a function of $1 - \Omega$. Our model results instead show an abrupt change in the balance of precipitation to dissolution at $\Omega = 0.7$. Once r_{fb} becomes larger than 10, precipitation accounts for only 10% or less of the net dissolution rate. Changes in r_{fb} therefore have a relatively small effect on the goodness of fit to the experimental data, and model fits with high r_{fb} accommodate a larger acceptable range in r_{fb}. Such an abrupt shift in the balance of precipitation to dissolution helps to explain the strongly nonlinear dissolution rates observed in many seawater calcite dissolution studies (e.g., refs. 6 and 7). It also implies a distinct change in dissolution mechanism.

Catalysis via Carbonic Anhydrase and a Link Between Solution Chemistry and Surface Features

The nonlinearity of a gross dissolution flux brings into question the chemical reactions responsible for calcite dissolution in seawater. In dilute solution, three calcite dissolution mechanisms are proposed to operate at the calcite surface (12, 16). Water-catalyzed dissolution is predicted to be independent of solution chemistry (the activity of the solid is always assumed to be 1). At low pH (<5), calcite dissolution depends almost exclusively on the transport of hydrogen ion to the mineral surface (14, 16, 29). CO_2 itself is thought to be relatively unreactive with $CaCO_3$, but H_2CO_3, produced through the hydration of CO_2, is an uncharged species that acts as a proton donor to promote dissolution (16, 29, 30).

There is increasing evidence that CA, an enzyme that catalyzes the equilibration of CO_2 and H_2CO_3, can enhance the dissolution rate of calcium carbonate in karst systems and their analogs

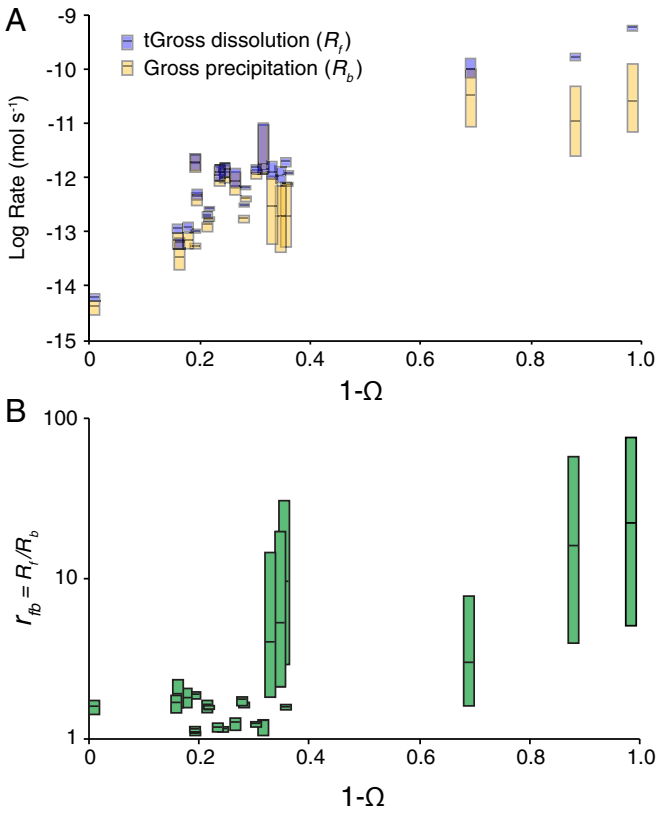

Fig. 3. Results of the dissolution–precipitation model. (*A*) Each net dissolution rate is represented by a pair of blue (dissolution) and yellow (precipitation) gross rates. Lines in the boxes are the median of the best fits of R_f; box boundaries are the 25th and 75th percentile values for R_f that best fit the experimental moles dissolved versus time data. Gross precipitation rates R_b are the median R_f divided by the median $r_{fb}(=R_f/R_b)$ of the best fits to the experimental data; box boundaries are the 25th and 75th percentile values for R_b. Overall, dissolution and precipitation rates are very close to each other, leading to a net dissolution rate that is the difference between two large gross fluxes. The precipitation rate variance increases (larger yellow box size) after $1-\Omega \approx 0.3$. (*B*) Box plot of the best-fitting r_{fb} values for the all experiments without CA. A significant jump in r_{fb} is evident after $1-\Omega \approx 0.3$ in both the absolute value of r_{fb} and the range of acceptable values.

(31–35). These studies used an open-system dissolution reactor, in which CO_2 gas was bubbled into an experimental chamber. There are two effects of CA in such a system. The first is rapid equilibration of the bubbled gas and the solution pCO_2, resulting in an experimental system limited by the kinetics of gas exchange and with a poorly constrained saturation state, as documented by ref. 16. Second, CA could enhance chemical mechanisms acting at the calcite–water interface. Our results are from closed-system dissolution experiments that have no headspace and thus isolate this second chemical mechanism of CA on calcite dissolution (ref. 9 and *Methods*).

Mass- and surface area-normalized dissolution rates from many ^{13}C dissolution experiments are plotted as a function of undersaturation ($1-\Omega$) and CA concentration in Fig. 4. Calcite dissolution rates in the presence of CA are always enhanced over the uncatalyzed rates. An experiment performed in the presence of BSA showed no significant enhancement of dissolution rate (*SI Appendix*, Fig. S9), demonstrating that proteinaceous dissolved organic matter has no significant effect on dissolution rate.

Increasing [CA] enhances dissolution at all saturation states, and CA has the largest effect close to equilibrium. Far-from-equilibrium enhancement of dissolution rate in Fig. 4, *Inset* shows similar rate enhancements to values obtained in freshwater experiments (31). This result is surprising, because many studies in freshwater have either dismissed carbonic acid as a major proton donor (7, 29) or have not found catalysis via CA in freshwater at low pCO_2 (31). Our documented rate increase of ~ 2.5 orders of magnitude at [CA] = 0.04 mg/mL and $\Omega \approx 0.85$ suggests that, in contrast to freshwater, carbonic acid is a major proton donor close to equilibrium in seawater.

The strong nonlinearities in our dissolution rate data cannot be explained using the simple dissolution framework of Eq. **1**. Furthermore, the addition of CA, although it increases the dissolution rate of calcite, does not produce a linear response of dissolution rate to saturation state. We were thus compelled to apply a model of dissolution to our rate data that incorporates features of the calcite solid into the control of dissolution rates (17, 21, 22, 36). For many solid–solution systems, a description of solution chemistry alone is indeed insufficient to predict crystal growth or dissolution kinetics. In addition to saturation state and its contribution to free energy, the crystal growth theory of ref. 37 incorporates energetics associated with the crystal itself, such as the free energy of crystal edges, faces, and lattice defects in contact with the solution. Recently, several studies have successfully mapped this theory of crystal growth and precipitation onto the dissolution of quartz, feldspar, diopside, and calcite (21, 36, 38). This model relates net dissolution rate (R_{diss}) to several physical–chemical parameters (h, ω, C_e, and a; see *SI Appendix*), as well as the dissolution velocity β at defects, surface defect density n_s, and the interfacial energy barrier at nucleation sites α (21, 39),

$$\ln\left[\frac{|R_{diss}|}{(1-\Omega)^{2/3}|\sigma|^{1/6}}\right] = \ln[h\beta C_e(\omega^2 h n_s a)^{1/3}] - \frac{\pi\alpha^2\omega h}{3(k_B T)^2}\left|\frac{1}{\sigma}\right|. \quad [2]$$

Saturation state control is found in the Ω and $\sigma = ln(\Omega)$ terms; $k_B T$ is the Boltzmann constant multiplied by temperature in kelvins, i.e., the system's thermal energy.

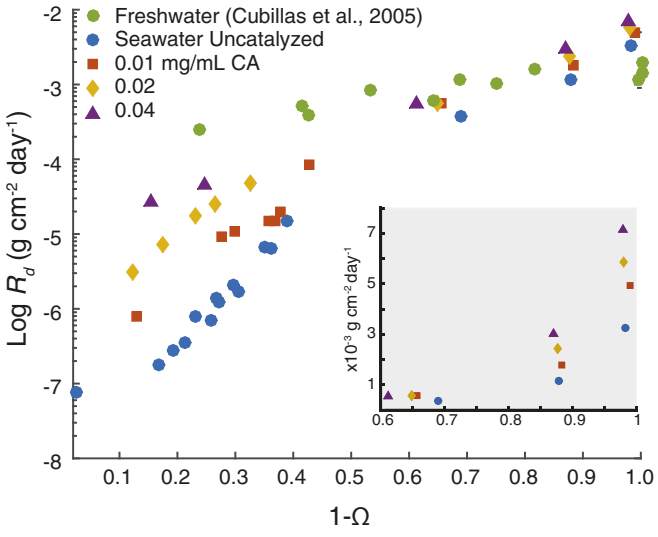

Fig. 4. The relationship between saturation state, carbonic anhydrase concentration, and calcite dissolution rate in seawater. Semilog plot of dissolution rate versus undersaturation ($1-\Omega$), including freshwater data from ref. 10. The linear–linear *Inset* at bottom right shows the far-from-equilibrium dissolution rate increase as a function of carbonic anhydrase. The *x* axis ($1-\Omega$) is the same as in the main figure; the *y* axis (dissolution rate) is in units of 10^{-3}g·cm^{-2}·d^{-1}. For clarity, *Inset* does not show freshwater data.

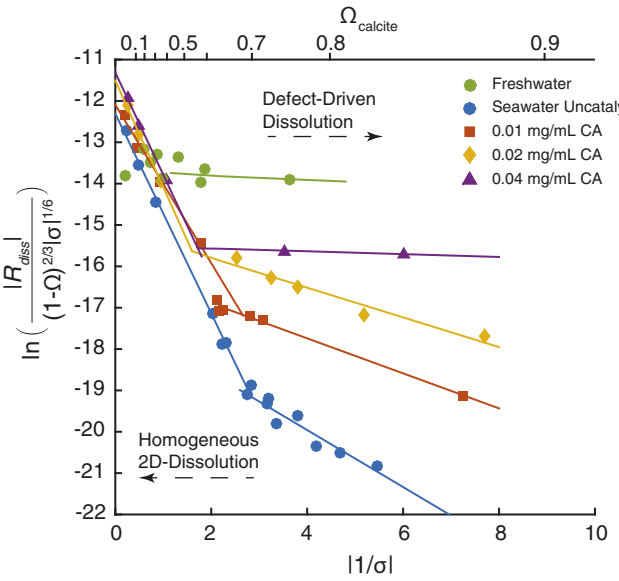

Fig. 5. Dissolution rate data from Fig. 4 plotted in the framework of Eq. **2**. The *y* axis dissolution rate (R_{diss}) is in moles per square meter per second. A top axis of corresponding Ω values is included, and regimes of dissolution with their hypothesized mechanisms are shown. To the right of the kink (closer to equilibrium), note the decreasing slope with increasing [CA]. Freshwater data are included for comparison. Linear fits to the data in this framework are presented in Table 1, along with an estimate of the interfacial surface energy α. The kink in these data represents a change in dissolution mechanism from defect-only nucleated dissolution near equilibrium to homogeneous nucleation far from equilibrium at a kink point around $\Omega = 0.7$.

Catalyzed and uncatalyzed dissolution rate data are plotted as the left-hand side of Eq. **2** versus $|1/\sigma|$ in Fig. 5, where $|1/\sigma| = 0$ is complete undersaturation. The slope of a straight line in this space gives the interfacial energy barrier α; the intercept gives information about the kinetic rate constant β and density of etch pit nucleation sites n_s. As seen in several other mineral dissolution studies (21, 22, 40), our uncatalyzed data plot as two straight lines in this space with a "kink" at $|1/\sigma| = 3$, which corresponds to $\Omega = 0.71$. This transition in slope denotes two distinct regimes of dissolution, which has been interpreted previously as a transition from defect-assisted nucleation of etch pits near equilibrium to homogeneous etch pit nucleation farther from equilibrium (21). It could also be interpreted as a transition from the opening of hollow cores to the propagation of step waves in the framework of Lasaga and Luttge (36). This transition to homogeneous nucleation of etch pits is also concurrent with the saturation state at which precipitation becomes unimportant to the overall dissolution rate in our $\delta^{13}C$ tracer data (Fig. 3).

Near equilibrium (to the right in Fig. 5), slopes decrease with increasing [CA] (Table 1). The slope of this line is diagnostic of the rate-limiting step in calcite dissolution near equilibrium. A decrease in the free energy barrier as a function of [CA] suggests that a greater availability of carbonic acid effectively decreases the energetic barrier to etch pit nucleation, by increasing the concentration of carbonic acid at defects on the calcite surface. The addition of CA also increases the intercept (Table 1), changing either the density of nucleation sites (n_s) or the rate of step retreat (β; Eq. **2**). Adding CA does not seem to significantly change the transition between defect-assisted and homogeneous nucleation: The kink point in Fig. 5 does not move significantly given the density of our data. The transition between these two regimes may be controlled instead by calcite saturation state (i.e., $[CO_3^{2-}]$). Because the kinetic interconversion of CO_2 and H_2CO_3 does not change the thermodynamic saturation state Ω, one might not expect this kink point to change significantly due to enhanced hydration kinetics. Far from equilibrium (to the left in Fig. 5), slopes are insensitive to [CA], indicating that interface energies at etch pit nucleation sites are insensitive to the concentration of H_2CO_3. Instead, transport of H_2CO_3 simply limits the delivery of protons to the mineral surface, limiting the overall propagation of etch pits once formed (i.e., modulating β or n_s in Eq. **2**).

A transition to homogeneous etch pit nucleation is also consistent with the mechanism shift diagnosed using relative dissolution and precipitation fluxes above. It is possible that precipitation limits net dissolution near equilibrium by occupying sites that would otherwise dissolve. This constraint is freed when etch pits begin to form everywhere on the solid surface. Instead of being limited to defects, dissolution is now allowed to proceed everywhere on the mineral surface, which erases the influence of precipitation reactions on the isotopic composition of the solid, and on the time-evolving solution $\delta^{13}C$.

Conclusion

In general, calcites react much more slowly and with less predictability in seawater than in freshwater, a problem that has plagued marine chemists for decades. Furthermore, calcite dissolution repeatedly has been shown to respond nonlinearly to saturation state, implying the presence of multiple dissolution mechanisms. We show here that this strongly nonlinear dissolution behavior in seawater is due to the combined effects of solution chemistry and geometric constraints on the propagation of dissolution features on the solid surface. Gross precipitation and dissolution fluxes influence the incorporation of both cation and anion tracers into the calcite solid. Treatment of bulk rate data using our box model demonstrates a change in the balance of dissolution and precipitation at $\Omega = 0.7$. Despite the chemical complexities that arise in seawater, our results suggest that carbonic acid availability is key, such that increasing its formation using CA drastically increases calcite dissolution near equilibrium. This reaction pathway appears to be rate-limiting in seawater near equilibrium. Incorporation of geometric constraints

Table 1. Fits for dissolution rate data shown in Fig. 5 in the framework of Eq. 2

	Near equilibrium			Far from equilibrium		
Experiment	Intercept	Slope	α, mJ·m^{-2}	Intercept	Slope	α, mJ·m^{-2}
SW Uncat.	−17.2 ± 0.5	−0.69 ± 0.11	15 ± 1.5	−12.3 ± 0.1	−2.4 ± 0.1	29 ± 1
0.01 mg/mL CA	−16.0 ± 0.1	−0.42 ± 0.02	12 ± 0.5	−12.1 ± 0.2	−1.9 ± 0.1	26 ± 2
0.02 mg/mL CA	−15.1 ± 0.2	−0.35 ± 0.05	11 ± 1.5	−11.5 ± 0.1	−2.6 ± 0.2	30 ± 2
0.04 mg/mL CA	−15.5	−0.03	3	−11.3 ± 0.1	−2.5 ± 0.1	29 ± 2
Freshwater (10)	−13.7 ± 0.3	−0.05 ± 0.15	4 ± 13			

Near-equilibrium fit data from $1/\sigma > 3$; far-from-equilibrium fits are from $0 < 1/\sigma < 3$. There are no errors on the 0.04 mg/mL data near equilibrium because the fit was made with two points. Freshwater data were taken from ref. 10. Only a single fit was performed on freshwater data, due to the lack of kink.

on dissolution rates suggests that the balance of precipitation and dissolution reactions changes fundamentally once etch pits freely nucleate and propagate across the calcite surface. These findings have implications not only for the reactivity differences of calcite between freshwater and seawater but also for how calcite dissolves in natural environments in the presence of increased CO_2 and carbonic anhydrase.

Methods

For dissolution rate measurements, we followed the methods detailed in ref. 9. More details can be found in *SI Appendix*. Briefly, ^{13}C-labeled carbonates were placed in undersaturated seawater in gas-impermeable bags with no headspace. The seawater was sampled over time for its DIC and $\delta^{13}C$, measured on a modified Picarro cavity ringdown spectrometer (CRDS) with Liason autosampler. The $\delta^{13}C$ signals were then converted into the number of moles dissolved versus time. Saturation state was measured by measuring DIC and total alkalinity on seawater before, during, and after every experiment. Solutions of lyophilized carbonic anhydrase from bovine erythrocites purchased from Sigma Aldrich (C2624) were made up in either deionized water or seawater. These solutions were added to the dissolution experiments to bring the total [CA] in each experiment to 0, 0.01, 0.02, or 0.04 mg/mL. Final experimental alkalinities were always checked; in several experiments, the alkalinity of initial experimental seawater was checked after CA addition to confirm the magnitude of alkalinity change due to CA. Dissolution rates calculated in this way were plotted against calculated saturation state and carbonic anhydrase concentration. Details on the box model and SIMS analysis can be found in *SI Appendix*.

ACKNOWLEDGMENTS. We acknowledge Alex Gagnon for helpful discussions on the formulation of the box model, and Yunbin Guan for help with SIMS analysis. We also thank Sijia Dong for discussions in general about carbonate dissolution in seawater. We thank Mathis Hain and one anonymous reviewer, whose careful reading and detailed comments greatly improved this manuscript. Thanks go to National Science Foundation Graduate Research Fellowship Program and the Resnick Institute Graduate Fellowships for supporting A.V.S. and J.N. We acknowledge support from NSF Grants OCE1220600 and OCE1220302.

1. Feely RA (2004) Impact of anthropogenic CO_2 on the $CaCO_3$ system in the oceans. *Science* 305:362–366.
2. Archer D, Kheshgi H, Maier-Reimer E (1998) Dynamics of fossil fuel CO_2 neutralization by marine $CaCO_3$. *Global Biogeochem Cycles* 12:259–276.
3. Ilyina T, Zeebe RE (2012) Detection and projection of carbonate dissolution in the water column and deep-sea sediments due to ocean acidification. *Geophys Res Lett* 39:L06606.
4. Honjo S, Erez J (1978) Dissolution rates of calcium carbonate in the deep ocean; an in-situ experiment in the North Atlantic Ocean. *Earth Planet Sci Lett* 40:287–300.
5. Walter LM, Morse JW (1985) The dissolution kinetics of shallow marine carbonates in seawater: A laboratory study. *Geochim Cosmochim Acta* 49:1503–1513.
6. Keir RS (1980) The dissolution kinetics of biogenic calcium carbonates in seawater. *Geochim Cosmochim Acta* 44:241–252.
7. Berner RA, Morse JW (1974) Dissolution kinetics of calcium carbonate in sea water; IV, theory of calcite dissolution. *Am J Sci* 274:108–134.
8. Fukuhara T, Tanaka Y, Ioka N, Nishimura A (2008) An in situ experiment of calcium carbonate dissolution in the central Pacific Ocean. *Int J Greenhouse Gas Control* 2: 78–88.
9. Subhas AV, et al. (2015) A novel determination of calcite dissolution kinetics in seawater. *Geochimica Cosmochim Acta* 170:51–68.
10. Cubillas P, Köhler S, Prieto M, Chaïrat C, Oelkers EH (2005) Experimental determination of the dissolution rates of calcite, aragonite, and bivalves. *Chem Geol* 216:59–77.
11. Ries JB, Ghazaleh MN, Connolly B, Westfield I (2016) Impacts of seawater saturation state (Ω_A= 0.4–4.6) and temperature (10, 25 °C) on the dissolution kinetics of whole-shell biogenic carbonates. *Geochim Cosmochim Acta* 192:318–337.
12. Plummer LN, Wigley T (1976) The dissolution of calcite in CO_2-saturated solutions at 25° C and 1 atmosphere total pressure. *Geochim Cosmochim Acta* 40:191–202.
13. Sjöberg EL (1976) A fundamental equation for calcite dissolution kinetics. *Geochim Cosmochim Acta* 40:441–447.
14. Sjöberg EL, Rickard DT (1984) Calcite dissolution kinetics: Surface speciation and the origin of the variable pH-dependence. *Chem Geol* 42:119–136.
15. Van Cappellen P, Charlet L, Stumm W, Wersin P (1993) A surface complexation model of the carbonate mineral-aqueous solution interface. *Geochim Cosmochim Acta* 57:3505–3518.
16. Arakaki T, Mucci A (1995) A continuous and mechanistic representation of calcite reaction-controlled kinetics in dilute solutions at 25°C and 1 atm total pressure. *Aquat Geochem* 1:105–130.
17. Teng HH (2004) Controls by saturation state on etch pit formation during calcite dissolution. *Geochim Cosmochim Acta* 68:253–262.
18. Arvidson RS, Fischer C, Lüttge A (2015) Calcite dissolution kinetics. *Aquat Geochem* 21:415–455.
19. Arvidson RS, Lüttge A (2010) Mineral dissolution kinetics as a function of distance from equilibrium – New experimental results. *Chem Geol* 269:79–88.
20. Xu J, Fan C, Teng HH (2012) Calcite dissolution kinetics in view of Gibbs free energy, dislocation density, and pCO_2. *Chem Geol* 322–323:11–18.
21. Dove PM, Han NZ, De Yoreo JJ (2005) Mechanisms of classical crystal growth theory explain quartz and silicate dissolution behavior. *Proc Natl Acad Sci USA* 102:15357–15362.
22. Dove PM, Han N, Wallace AF, De Yoreo JJ (2008) Kinetics of amorphous silica dissolution and the paradox of the silica polymorphs. *Proc Natl Acad Sci USA* 105:9903–9908.
23. Zhong S, Mucci A (1989) Calcite and aragonite precipitation from seawater solutions of various salinities: Precipitation rates and overgrowth compositions. *Chem Geol* 78:283–299.
24. Schrag DP, DePaolo DJ, Richter FM (1995) Reconstructing past sea-surface temperatures: Correcting for diagenesis of bulk marine carbonate. *Geochim Cosmochim Acta* 59:2265–2278.
25. Gorski CA, Fantle MS (2017) Stable mineral recrystallization in low temperature aqueous systems: A critical review. *Geochim Cosmochim Acta* 198:439–465.
26. Richter FM, DePaolo DJ (1987) Numerical-models for diagenesis and the Neogene sr isotopic evolution of seawater from DSDB site 590B. *Earth Planet Sci Lett* 83:27–38.
27. Emerson S, Bender M (1981) Carbon fluxes at the sediment-water interface of the deep-sea: Calcium carbonate preservation. *J Mar Res* 39:139–162.
28. Boudreau BP (2013) Carbonate dissolution rates at the deep ocean floor. *Geophys Res Lett* 40:744–748.
29. Plummer LN, Wigley T, Parkhurst DL (1978) The kinetics of calcite dissolution in CO_2-water systems at 5° to 60°C and 0.0 to 1.0 atm CO_2. *Am J Sci* 278:179–216.
30. Dreybrodt W, Lauckner J, Zaihua L, Svensson U (1996) The kinetics of the reaction $CO_2+H_2O \rightarrow H^+ + HCO_3^-$ as one of the rate limiting steps for the dissolution of calcite in the system H_2O-CO_2-$CaCO_3$. *Geochim Cosmochim Acta* 60:3375–3381.
31. Liu Z, Yuan D, Dreybrodt W (2005) Comparative study of dissolution rate-determining mechanisms of limestone and dolomite. *Environ Geol* 49:274–279.
32. Zaihua L (2001) Role of carbonic anhydrase as an activator in carbonate rock dissolution and its implication for atmospheric CO_2 sink. *Acta Geol Sin* 75:275–278.
33. Thorley RMS, Taylor LL, Banwart SA, Leake JR, Beerling DJ (2014) The role of forest trees and their mycorrhizal fungi in carbonate rock weathering and its significance for global carbon cycling. *Plant Cell Environ* 38:1947–1961.
34. Xie T, Wu Y (2013) The role of microalgae and their carbonic anhydrase on the biological dissolution of limestone. *Environ Earth Sci* 71:5231–5239.
35. Li W, et al. (2008) Limestone dissolution induced by fungal mycelia, acidic materials, and carbonic anhydrase from fungi. *Mycopathologia* 167:37–46.
36. Lasaga AC, Luttge A (2001) Variation of crystal dissolution rate based on a dissolution stepwave model. *Science* 291:2400–2404.
37. Burton WK, Cabrera N, Frank FC (1951) The growth of crystals and the equilibrium structure of their surfaces. *Phil Trans R Soc Lond Ser A Math Phys Sci* 243:299–358.
38. Dixit S, Carroll SA (2007) Effect of solution saturation state and temperature on diopside dissolution. *Geochem Trans* 8:3–14.
39. Sangwal K (1987) *Etching of Crystals: Theory, Experiment, and Application* (North Holland, Amsterdam).
40. Malkin AI, Chernov AA, Alexeev IV (1989) Growth of dipyramidal face of dislocation-free ADP crystals - free-energy of steps. *J Cryst Growth* 97:765–769.